Check for updates

Angewandte Chemie International Edition

Angewandte International Edition Chemie

GDCh German Chemical Society

How to cite: *Angew. Chem. Int. Ed.* **2026**, e2278978
doi.org/10.1002/anie.2278978

RESEARCH ARTICLE Hot Paper

Atomic-Precision Engineering and Visualizing of Chiral Electronic States in Nitrogen-Doped Nanographenes

Zhi-Hao Li[1,3] | Jia-Qi Dai[1,2] | Guan Luo[1,3] | Ruo-Ning Li[1] | An-Jing Zhao[1] | Jun-Jie Duan[1] | Yu Ge[1,3] | Zi-Cong Wang[1,3] | Wei Ji[2] | Ting Chen[1] | Dong Wang[1,3] | Li-Jun Wan[1,3]

[1]CAS Key Laboratory of Molecular Nanostructure and Nanotechnology, CAS Research/Education Center For Excellence in Molecular Sciences, Beijing National Laboratory For Molecular Science (BNLMS), Institute of Chemistry, Chinese Academy of Sciences, Beijing, P. R. China | [2]Beijing Key Laboratory of Optoelectronic Functional Materials & Micro-Nano Devices, Key Laboratory of Quantum State Construction and Manipulation (Ministry of Education) School of Physics, Renmin University of China, Beijing, P. R. China | [3]School of Chemical Sciences, University of Chinese Academy of Sciences, Beijing, P. R. China

Correspondence: Wei Ji (wji@ruc.edu.cn) | Ting Chen (chenting@iccas.ac.cn)

Received: 11 January 2026 | **Revised:** 9 April 2026 | **Accepted:** 13 April 2026

Keywords: chiral electronic structures | nanographenes | nitrogen-doping | on-surface synthesis | scanning tunneling microscopy

ABSTRACT

As a fundamental phenomenon in nature, chirality has been extensively studied in molecular structures; however, it remains underexplored at the electronic level. Understanding how structural chirality transfers into electronic states is crucial for uncovering the essence of many chiral effects. In this study, we report the engineering and direct visualization of chiral electronic states within an otherwise planar, achiral hexa-*peri*-hexabenzocoronene (HBC) framework. By employing atomically precise asymmetric nitrogen doping of HBC through on-surface synthesis, we fabricate a C_3-symmetric triaza-HBC on Au(111). Utilizing high-resolution scanning tunneling microscopy and non-contact atomic force microscopy, we resolve the chiral molecular structure of triaza-HBC confined to the surface, as well as the chiral texture of the resulting interfacial electronic states and its evolution at different energies. Density functional theory calculations reveal that these electronic chiral features arise from the molecule's intrinsic chiral orbitals, which hybridize strongly with the metal substrate while still retaining their chiral character. This study not only demonstrates a clear transfer of chirality from molecular structure to the electronic landscape but also provides a versatile platform for the rational design of chiral electronic molecules and materials.

1 | Introduction

Chirality, a fundamental form of asymmetry, governs critical phenomena across biology, chemistry, physics, and material science [1–4]. Extensive research has focused on the expression and control of structural chirality that manifests in the asymmetric spatial arrangement of atoms and molecules [5]. However, chirality can also emerge in electronic structures, specifically in the form of chiral orbitals for molecules [6]. These chiral orbitals play a crucial role in enabling molecules to perform their functions in many enantioselective processes [7–10]. For example, in chiral catalysis, the asymmetric overlap of orbitals between the catalyst and reactant dictates both the reaction energy barrier and the enantioselectivity [8]. Therefore, studying chiral molecular orbitals is of significance for advancing our mechanistic understanding from a geometric to an electronic perspective, as well as for facilitating the rational design of chiral functional molecules and materials.

Zhi-Hao Li and Jia-Qi Dai contributed equally to this work.

© 2026 Wiley-VCH GmbH

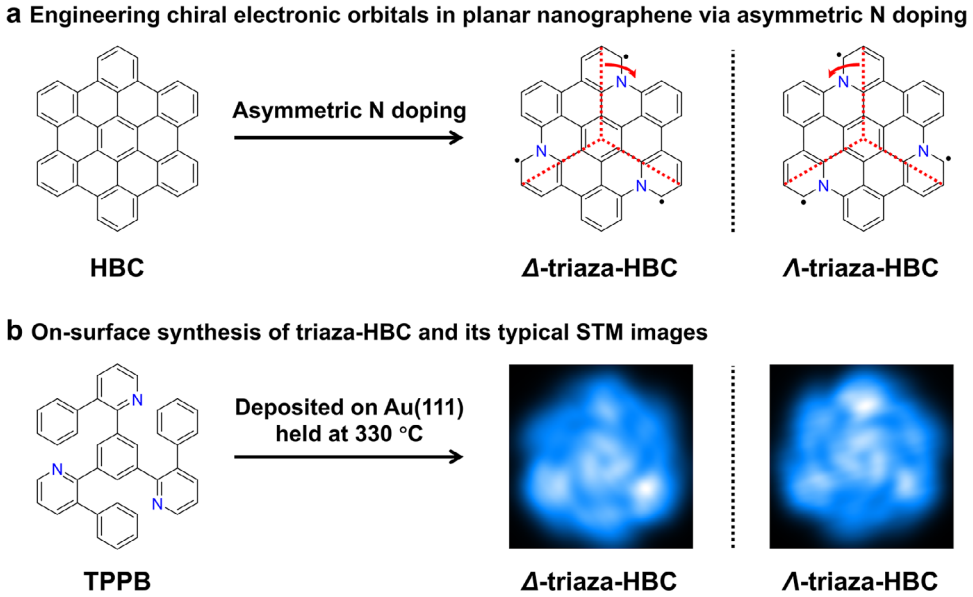

FIGURE 1 | Engineering chiral electronic orbitals in planar nanographene. (a) Design principle: Inducing chirality into planar HBC through asymmetric nitrogen doping. The handedness of the molecules is defined by the rotation orientation of the nitrogen atoms relative to the line connecting the pyridine ring and the central benzene ring (indicated by red dashed lines). Clockwise and anticlockwise rotations correspond to the *Δ*- and *Λ*-enantiomer, respectively. DFT calculations indicate triaza-HBC possesses a quartet ground state, where the unpaired electrons delocalize within the π system. Here, we just give one of the resonance structures of triaza-HBC. (b) On-surface synthesis of triaza-HBC from TPPB and typical STM images.

In principle, structurally chiral molecules inherently possess chiral molecular orbitals [11]. The interactions of these chiral molecular orbitals with external entities like reactants, detection probes, or photons are crucial in determining functions across various applications, including chiral catalysis [12], sensing [13–15], and photonics [16–18]. However, the direct characterization of these chiral molecular orbitals is experimental challenging. Scanning tunneling microscopy (STM) offers a powerful tool in this regard. It allows for atomic-resolution imaging of molecular structures [19]. Moreover, by using scanning tunneling spectroscopy (STS), it is possible to map the local density of electronic states [20], thereby enabling real-space visualization of the shape and spatial distribution of chiral molecular orbitals [21, 22]. Recent STM/STS studies have revealed chiral features in the frontier molecular orbitals of structurally chiral molecules [23–25]. Chiral molecular orbitals induced by asymmetric charge transfer have also been imaged in achiral porphyrins adsorbed on surfaces or on molecular assemblies [26, 27]. Additionally, chiral charge-density waves have been observed in 2D materials [28]. These advances shed light on the emergence of chiral electronic structures, yet fundamental questions remain regarding the precise correlation between chiral molecular structures and their orbital characteristics, the energy-dependent evolution of these orbitals, and their interactions with external entities.

In this study, we demonstrate the engineering of chiral electronic orbitals in an otherwise planar, achiral hexa-*peri*-hexabenzocoronene (HBC) molecule through asymmetric nitrogen doping (Figure 1a). Our design principle is based on the well delocalized π-electron system of HBC and the distinct electronegativity of nitrogen compared to carbon. Replacing carbon with nitrogen atoms at asymmetric positions is expected to break both the geometric symmetry and the π-electron density distribution of HBC. We employ an on-surface synthesis strategy, which has been successfully utilized to construct heteroatom-doped carbon nanostrucutres [29–33], to achieve atomically precise incorporation of nitrogen atoms into the HBC skeleton. As illustrated, the precursor 1,3,5-tris(3-phenylpyridin-2-yl)benzene (TPPB) undergoes intramolecular C—C and C—N coupling upon deposited onto Au(111) surface held at 330°C (Figure 1b). Using high-resolution STM and non-contact atomic force microscopy (*nc*-AFM), we identify the two enantiomers of the resulting triaza-HBC (*Δ*- and *Λ*-). Furthermore, we directly visualize several windmill-like interfacial electronic states near the Fermi level, whose chiral features evolve with bias energy. Density functional theory (DFT) calculations confirm that these chiral interfacial electronic states arise from hybridization between the intrinsic chiral molecular orbitals of triaza-HBC and the Au substrate. This work demonstrates direct transfer of chirality from molecular structure to molecular orbitals and interfacial electronic states. It establishes precisely asymmetric nitrogen doping via on-surface synthesis as an effective routine to engineer chiral electronic structures in π-electron systems.

2 | Results and Discussion

Figure 2a displays a hexagonal porous network formed by TPPB on Au(111) surface held at room temperature. Each molecule has three bright protrusions, corresponding to its lateral phenyl groups that are tilted with respect to the substrate. These distinctive features enable discrimination of the two enantiomers, *Δ*- and *Λ*-TPPB, as indicated in the corresponding STM images (Figure 2b,c). It is suggested that the hexagonal porous networks consist exclusively of either *Δ*- or *Λ*-TPPB. DFT-optimized adsorption geometry indicates that TPPB adsorbs with its central benzene ring positioned atop a gold atom on the Au(111) surface (Figures 2d and S1). The central benzene and the pyridine rings

15213773, 0, Downloaded from https://onlinelibrary.wiley.com/doi/10.1002/anie.202278978 by Wei Ji - RENMIN UNIVERSITY OF CHINA NON-EAL ACCOUNT , Wiley Online Library on [24/04/2026]. See the Terms and Conditions (https://onlinelibrary.wiley.com/terms-and-conditions) on Wiley Online Library for rules of use; OA articles are governed by the applicable Creative Commons License

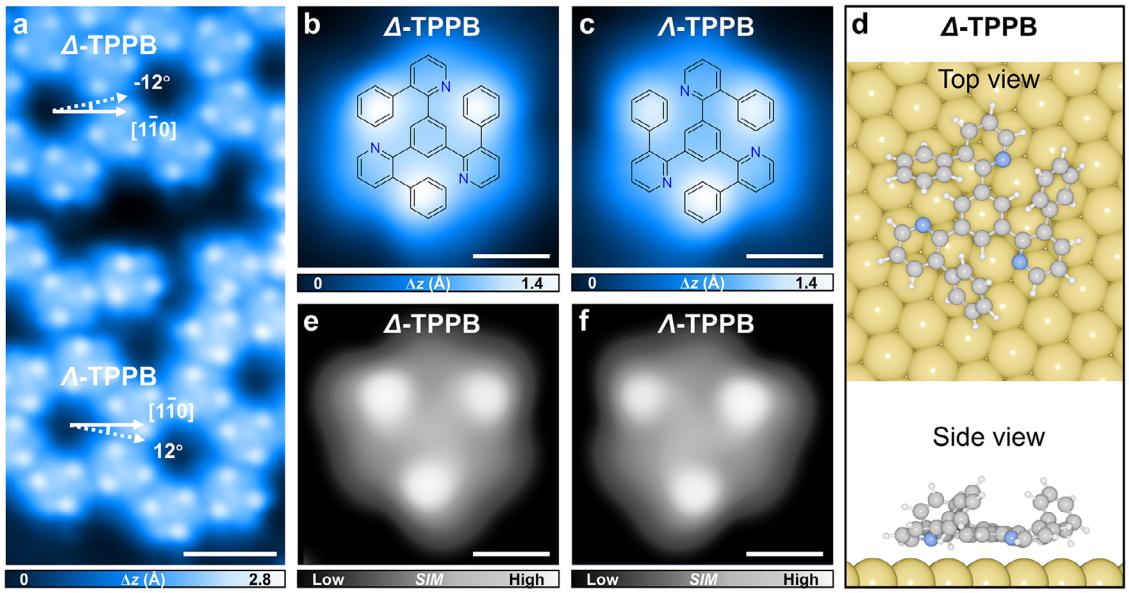

FIGURE 2 | Adsorption of TPPB precursors on Au(111). (a) STM image of hexagonal porous structures formed by TPPB on Au(111). $V_s = 1.7$ V, $I_t = 100$ pA. (b and c) High-resolution STM images of individual *Δ*- and *Λ*-TPPB. $V_s = -1.0$ V, $I_t = 80$ pA. (d) DFT-optimized adsorption geometry of *Δ*-TPPB on Au(111). (e and f) Simulated STM images of *Δ*- and *Λ*-TPPB on Au(111). Scale bars: (a) 20 Å, (b,c,e,f) 5 Å.

adopt nearly planar orientations relative to the surface, while the lateral phenyl groups are tilted upward. Simulated STM images of *Δ*-TPPB and *Λ*-TPPB (Figure 2e,f) based on the DFT-optimized geometries show excellent agreement with the experimental observations.

To pursue the synthesis of triaza-HBC, TPPB molecules were deposited onto a preheated Au(111) surface. Figure 3a shows an STM image of the outcomes obtained at 330°C. The TPPB precursors characterized by bright protrusions are no longer observed on the surface. Instead, regular hexagram-shaped motifs identified as triaza-HBC molecules are observed (depicted in Figure 3a). The triaza-HBC molecules are oriented at −15° or +15° relative to the [1–10] direction of the Au(111) substrate. The molecules exhibit C_3 symmetry, a reduction from the inherent D_{6h} symmetry of the parent HBC due to asymmetric nitrogen incorporation. We explored a series of substrate temperatures and found that optimizing the annealing temperature does not favor the formation of the intact triaza-HBC molecule (Figure S4). The yield of intact triaza-HBC on the surface remains very low even at the optimized reaction temperature (Figure S5). The molecule tends to undergo ring-contraction reactions, forming byproduct that contains aza-five-membered rings (Figure S6). These byproducts further undergo intermolecular coupling, leading to covalent dimers (Figure S7) or short irregular oligomers. This behavior is likely due to the high reactivity of the molecule, which originates from its open-shell character, as will be discussed in detail below.

High-resolution STM images reveal the chiral characteristics of triaza-HBC. As shown in Figure 3b,c, each triaza-HBC molecule consists of a central windmill-like unit and three isolated lobes positioned between the windmill blades. The windmill-like unit can rotate in either a clockwise or counterclockwise direction, clearly demonstrating the chirality of triaza-HBC. The molecular structures of triaza-HBC were elucidated using *nc*-AFM with a CO-functionalized tip. As shown in Figure 3d,e, the C—C bonds, including the newly formed ones (indicated by red arrows), are clearly resolved, while the C—N bonds cannot be identified clearly. This is because the nitrogen atoms embedded in the carbon framework appear as dark depressions, which is consistent with previous reports [34, 35]. Based on these features, the positions of the nitrogen atoms relative to the central benzene-pyridine axis can be determined, allowing the chirality of the molecules to be experimentally identified. It is demonstrated that the molecules oriented at −15° (Figure 3d) or +15° (Figure 3e) relative to the [1–10] direction of the Au(111) substrate correspond to *Δ*- or *Λ*-triaza-HBC, respectively. A comparison of the *nc*-AFM images of triaza-HBC with their molecular structures show good agreement (Figure S2). Furthermore, DFT optimized geometry of triaza-HBC on Au(111) indicates that the molecule adopts a planar adsorption configuration with its central phenyl ring atop an Au atom and its molecular axis offset by −15° (*Δ*-triaza-HBC, Figure 3f) or +15° (*Λ*-triaza-HBC, Figure S3) relative to the [1–10] direction of the Au(111) substrate. These characteristics are consistent with the experimental observations. Simulated STM (Figure 3g,h) and *nc*-AFM images (Figure 3i,j) of both *Δ*- and *Λ*-triaza-HBC based on the DFT-optimized geometries well match the corresponding experimental images. These findings further confirm the successful synthesis of triaza-HBC.

Interestingly, the chiral features of triaza-HBC are more clearly discernible in STM measurements conducted with a CO-functionalized tip. Figure 4a,c display constant-current STM images of *Δ*- and *Λ*-triaza-HBC obtained using a CO-functionalized tip. A chiral galaxy-like pattern is revealed, within which a small windmill-like chiral structure is clearly resolved at the molecular center. Additionally, the chiral pattern of triaza-HBC evolves with bias voltage (Figures S8 and S9). To gain deeper insight, we also recorded the constant-height STM images, as these provide more information about the electronic structures of a planar molecule. As shown in Figure 4b,d,

15213773, 0, Downloaded from https://onlinelibrary.wiley.com/doi/10.1002/anie.202578978 by Wei Ji - RENMIN UNIVERSITY OF CHINA NON-EAL ACCOUNT, Wiley Online Library on [24/04/2026]. See the Terms and Conditions (https://onlinelibrary.wiley.com/terms-and-conditions) on Wiley Online Library for rules of use; OA articles are governed by the applicable Creative Commons License

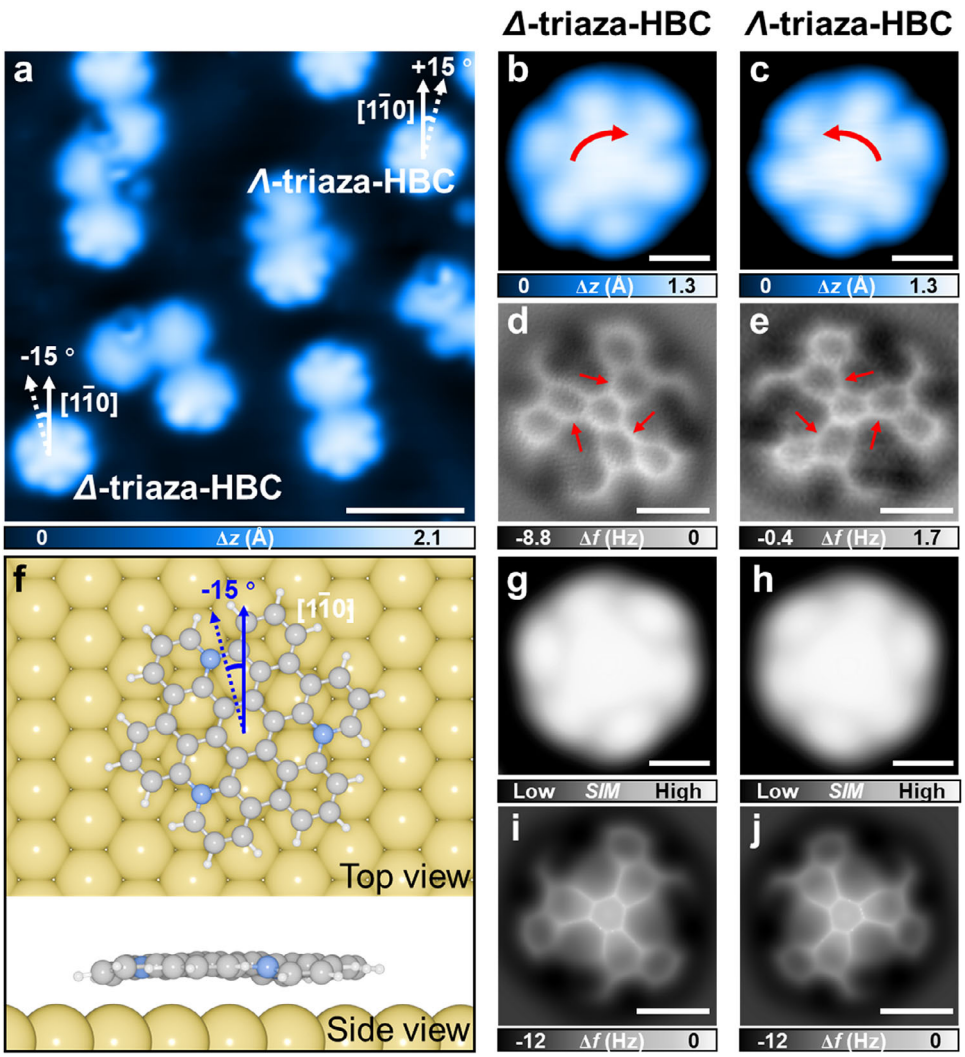

FIGURE 3 | Synthesis of triaza-HBC on Au(111). (a) Over-view STM image of the outcomes. $V_s = 500$ mV, $I_t = 200$ pA. (b and c) High-resolution STM images of *Δ*- and *Λ*-triaza-HBC. $V_s = 500$ mV, $I_t = 200$ pA. (d and e) nc-AFM images of *Δ*- and *Λ*-triaza-HBC. Open feedback parameters: $V_s = 100$ mV, $I_t = 100$ pA, $\Delta Z = -0.8$ Å. (f) DFT-optimized geometry of *Δ*-triaza-HBC on Au(111). (g and h) Simulated STM images of *Δ*- and *Λ*-triaza-HBC on Au(111). (i and j) Simulated nc-AFM images of *Δ*- and *Λ*-triaza-HBC on Au(111). Scale bars: (a) 20 Å, (b–e), (g–j) 5 Å.

constant-height STM images obtained with a CO-functionalized tip reveal obvious bias-dependent chiral features as well. These chiral patterns are well reproduced by PPSTM simulations using a mixed tip (5% *s* and 95% p_{xy}) (Figures S10 and S11) [36]. This evolution of chiral features with bias voltage indicates that the observed chirality is strongly influenced by electronic structural properties, rather than being solely determined by geometric asymmetry [37].

In the following, we focus on the electronic structures of triaza-HBC on Au(111), aiming to reveal the origin of the observed chiral characteristics in topographic STM images. Our dI/dV spectra acquired over *Δ*-triaza-HBC exhibit four distinct peaks centered at −0.30, 0.21, 0.45, and 1.36 V, labeled as P1, P2, P2, and P4, respectively (Figure 5a). Figure 5b shows the dI/dV maps recorded at these energies, which display asymmetric windmill-like spatial distributions. More importantly, the rotation direction of the windmill structures flips for different electronic states. The windmill structures of states P1, P2, and P3 rotate the same direction, while the structure of state P4 rotates opposite. These findings further verify that the chiral features observed in STM topographic images are associated with chiral electronic structures.

To assign the electronic states corresponding to the peaks in the STS spectra, we carried out spin-polarized DFT calculations of freestanding and adsorbed triaza-HBC molecule on Au(111). Figure 5c shows the spin-polarized density of states (DOS) of a freestanding *Δ*-triaza-HBC molecule, which exhibits an open-shell character with a total magnetic moment of 3.0 μB. The three unpaired electrons couple ferromagnetically and give a quartet ground state, in which the spin density is predominantly distributed around the nitrogen-containing heterocycles (Figure S12a). Many-body calculations using the complete active space self-consistent field (CASSCF) method reveal three natural orbitals with occupation number close to 1 (Figure S12b), further confirming its open-shell quartet state. The exchange coupling strength was estimated to be 21.8 meV (UDFT) and 12.0 meV (CASSCF) using a Heisenberg spin model for three triangle-arranged spins [38].

15213773, 0, Downloaded from https://onlinelibrary.wiley.com/doi/10.1002/anie.202518978 by Wei Ji - RENMIN UNIVERSITY OF CHINA NON-EAL ACCOUNT , Wiley Online Library on [24/04/2026]. See the Terms and Conditions (https://onlinelibrary.wiley.com/terms-and-conditions) on Wiley Online Library for rules of use; OA articles are governed by the applicable Creative Commons License

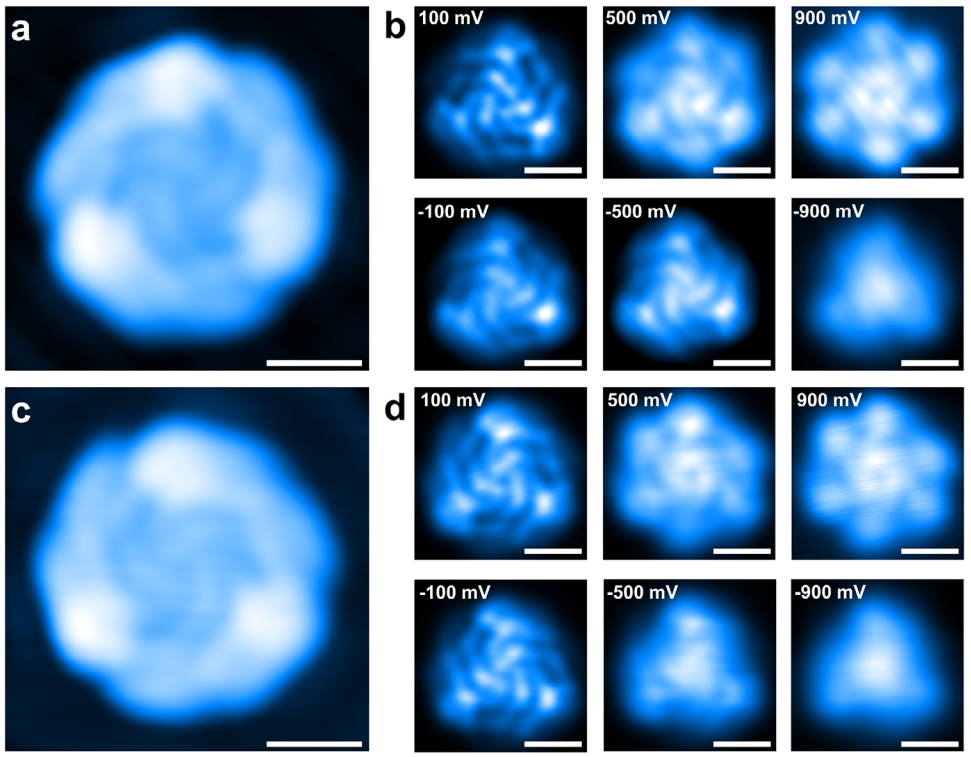

FIGURE 4 | STM images of triaza-HBC obtained with a CO-functionalized tip. (a and c) Constant-current STM image of *Δ*- and *Λ*-triaza-HBC. $V_s = 100$ mV, $I_t = 100$ pA. (b and d) Constant-height STM images of *Δ*- and *Λ*-triaza-HBC acquired at different bias voltages. Open feedback parameters: $I_t = 100$ pA; $\Delta Z = -0.6$ Å. Scale bars: 5 Å.

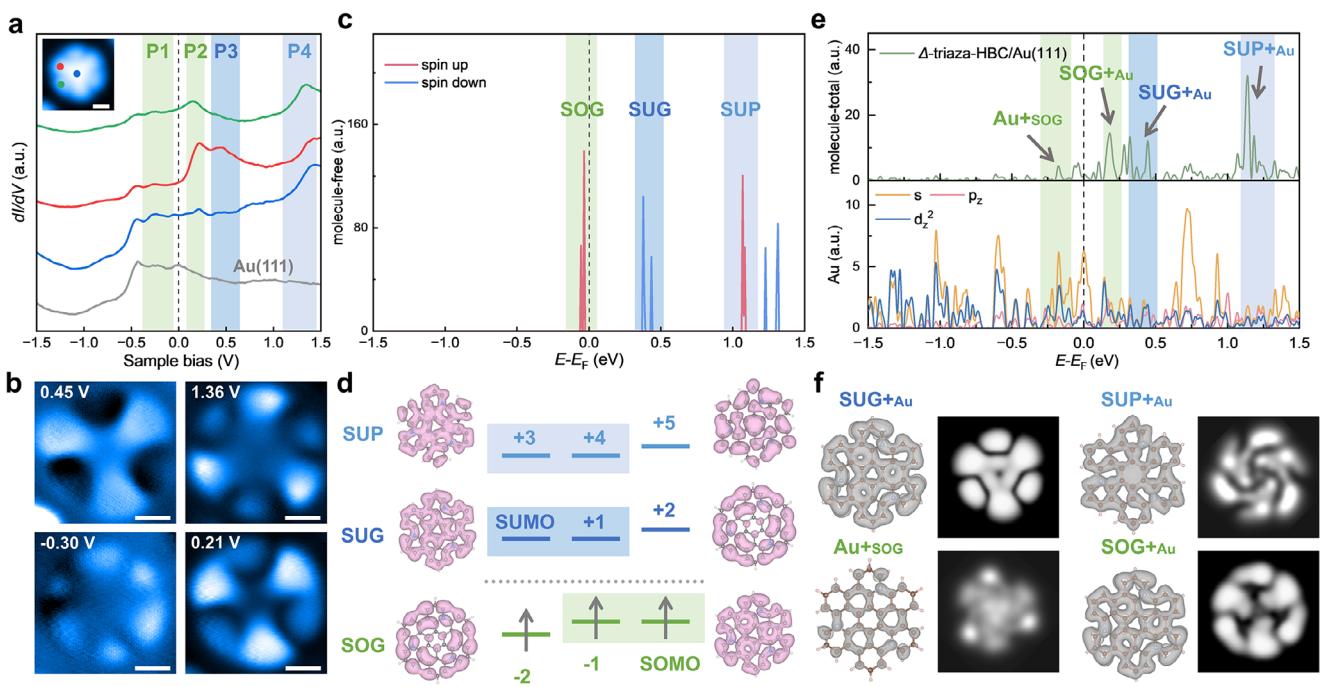

FIGURE 5 | Electronic structures and orbital characteristics of *Δ*-triaza-HBC. (a) Experimental dI/dV spectra of *Δ*-triaza-HBC on Au(111). Open feedback parameters: V_s = 800 mV, I_t = 300 pA, V_m = 30 mV, f = 843 Hz. (b) Constant-current dI/dV maps obtained at the corresponding energies. $I_t = 300$ pA, $V_m = 30$ mV, $f = 843$ Hz. (c) Spin-polarized DOS of the freestanding molecule. The SOG, SUG, and SUP are highlighted. (d) Schematic diagram of the frontier molecular orbitals with corresponding visualized wavefunction norms. The isosurface contours are 1×10^{-4} e/Bohr^3. (e) Calculated PDOS of the molecule (top) and the hybridized Au orbitals (bottom), showing four hybridized states (SOG, SUG and SUP with Au). (f) The corresponding visualized wavefunction norms and LDOS of four states. The isosurface contours are 1×10^{-4} e/Bohr^3. Scale bars: 5 Å.

15213773, 0, Downloaded from https://onlinelibrary.wiley.com/doi/10.1002/anie.202278978 by Wei Ji - RENMIN UNIVERSITY OF CHINA NON-EAL ACCOUNT , Wiley Online Library on [24/04/2026]. See the Terms and Conditions (https://onlinelibrary.wiley.com/terms-and-conditions) on Wiley Online Library for rules of use; OA articles are governed by the applicable Creative Commons License

The frontier orbitals of a freestanding Δ-triaza-HBC are illustrated in Figure 5d, as categorized into three characteristic groups. A singly occupied group (SOG), containing three orbitals, is located below the Fermi level; a singly unoccupied group (SUG) mirrors SOG in energy, residing above the Fermi level. Orbitals denoted by SOMO and SOMO-1, and by SUMO and SUMO+1 are degenerated with each other, respectively. These additional orbitals sitting at even higher positive energies are grouped into the SUMO plus set (SUP). All orbitals in these three groups exhibit pronounced chiral characteristics. Simulated LDOS of the freestanding molecule show that the electronic pattern of SUP exhibits opposite chirality to those of SOG and SUG (Figure S13). This finding aligns with the experimental observation that the chirality of state P4 is opposite to that of states P1, P2, and P3.

Upon adsorption on an Au(111) substrate, the magnetic moments of the triaza-HBC molecule are fully quenched, suggesting a singlet ground state (Figure S14). The frontier molecular orbitals strongly renormalize with energy shifting and broadening (Figure 5e), ascribed to their electronic hybridization with Au states underneath. Moreover, a net electron transfer from triaza-HBC to the Au substrate is revealed in charge density difference (Figure S15). Both effects likely contribute to the quenching of the molecular magnetic moments. By comparison of the theoretical projected density of states (PDOS) of the adsorbed molecule with the experimental STS spectra, the relatively broad and less pronounced P1 peak was assigned to hybridized states of Au *s* and d_{z^2} states with SOG, denoted Au+SOG and centered at approximately −0.3 eV. Their antibonding states, residing at around +0.2 eV, are predominately contributed by SOG, denoting SOG+Au, which corresponds to the experimental P2 peak. Experimental peaks P3 and P4 are primarily composed of SUG and SUP sets, with minor contributions from the substrate, denoted as SUG+Au and SUP+Au, respectively. Figure 5f illustrates the wavefunction-norm (for the Gamma point only) contours and simulated local density of states (LDOS) for peaks P1 to P4. The windmill-like features remain essentially consistent with those of the freestanding molecule (Figure 5d), suggesting that the adsorption does not modify the intrinsic chirality of the molecule. The calculated LDOS are in good agreement with the experimental dI/dV maps.

The dI/dV spectra and maps of Λ-triaza-HBC, along with the corresponding DFT calculation results, are shown in Figure S16. Similarly, peaks P1, P2, P2, and P4 are observed in the dI/dV spectra. Their corresponding dI/dV maps exhibit opposite chirality compared to those of Δ-triaza-HBC. DFT calculations performed for the Λ-triaza-HBC molecule at the same level yield analogous results. That is, the freestanding Λ-triaza-HBC molecule exhibit intrinsic chiral frontier molecular orbitals with handedness opposite to that of Δ-triaza-HBC. These chiral molecular orbitals hybridize with the Au substrate, giving birth to chiral interfacial electronic states with handedness identical to the molecular orbitals.

To further emphasize the role of molecular orbitals, rather than interaction with the substrate, in the observed chiral interfacial structures of triaza-HBC on Au(111), we performed the following additional calculations. First, we calculated another adsorption configuration oriented at an angle of +15° for Δ-triaza-HBC, as shown in Figure S17. The spin-averaged PDOS reveal that the presence of strong SOG-Au electronic hybridization is independent of detailed adsorption orientation. Although the intensity varies in some way, the overall chirality of the molecule remains the same as in the freestanding case, which indicates that the chirality of molecular states is also independent to the adsorption orientation. Second, we calculated the electronic structures of another triaza-HBC molecule with D_{3h}-symmetry, adsorbed on Au(111) in a similar adsorption site and orientation to those of Δ-triaza-HBC/Au(111) (Figure S18). The results indicate that the molecular orbitals of the D_{3h}-symmetric triaza-HBC molecule exhibit symmetric rather than chiral shapes. The simulated constant-height STM images with a CO-tip are also achiral, which further confirms the dominant role played by the molecule itself in exhibiting electronic chirality.

3 | Conclusion

In summary, we demonstrated the engineering of chiral electronic structures in a planar nanographene through a rational design and precise on-surface synthesis strategy. The incorporation of nitrogen atoms at asymmetric positions in the HBC skeleton not only breaks the geometric symmetry but effectively induces a distinct chiral electronic distribution. The direct real-space visualization of the resulting windmill-like chiral electronic states and their evolution with bias voltage, achieved via STM/STS and nc-AFM techniques, provides compelling evidence that the observed chirality is intrinsic to the electronic structures of the adsorbed molecules, rather than arising from geometric distortion. DFT calculations confirm that while hybridization with the Au(111) substrate leads to band renormalization and molecule–substrate charge transfer, the fundamental chiral character of the molecular orbitals is preserved. This work establishes a route to engineer and characterize chiral electronic states in low-dimensional materials. The demonstrated ability to tailor chiral electronic properties in a bottom-up manner opens new avenues for the development of functional materials and devices, with potential relevance to enantioselective catalysis, chiral spin electronics, and emerging quantum optical technologies.

Acknowledgements

This work was supported by the National Natural Science Foundation of China (92477207, 92477205, 22372175, 22421001 and 5246116032), the Strategic Priority Research Program of CAS (XDB0520201), and the National Key Research and Development Program of China (No. 2023YFB4006200 and No. 2023YFA1406500). Calculations were performed at the Physics Lab of High-Performance Computing (PLHPC) and the Public Computing Cloud (PCC) of Renmin University of China.

Conflicts of Interest

The authors declare no conflicts of interest.

Data Availability Statement

The data that support the findings of this study are available on request from the corresponding author. The data are not publicly available due to privacy or ethical restrictions.

15213773, 0, Downloaded from https://onlinelibrary.wiley.com/doi/10.1002/anie.202518978 by Wei Ji - RENMIN UNIVERSITY OF CHINA NON-EAL ACCOUNT , Wiley Online Library on [24/04/2026]. See the Terms and Conditions (https://onlinelibrary.wiley.com/terms-and-conditions) on Wiley Online Library for rules of use; OA articles are governed by the applicable Creative Commons License

References

1. L. T. Guo, Y. Q. Guo, R. Wang, et al., "Interface Chirality: From Biological Effects to Biomedical Applications," *Molecules (Basel, Switzerland)* 28 (2023): 5629, https://doi.org/10.3390/molecules28155629.

2. D. A. Nagib, "Asymmetric Catalysis in Radical Chemistry," *Chemical Reviews* 122 (2022): 15989–15992, https://doi.org/10.1021/acs.chemrev.2c00622.

3. F. Furlan, J. M. Moreno-Naranjo, N. Gasparini, S. Feldmann, J. Wade, and M. J. Fuchter, "Chiral Materials and Mechanisms for Circularly Polarized Light-emitting Diodes," *Nature Photonics* 18 (2024): 658–668, https://doi.org/10.1038/s41566-024-01408-z.

4. S. Stolz, M. Danese, M. Di Giovannantonio, et al., "Asymmetric Elimination Reaction on Chiral Metal Surfaces," *Advanced Materials* 34 (2021): 2104481, https://doi.org/10.1002/adma.202104481.

5. G. W. Li, Q. Yang, K. Manna, et al., "Observation of Asymmetric Oxidation Catalysis With B20 Chiral Crystals**," *Angewandte Chemie International Edition* 62 (2023): e202303296, https://doi.org/10.1002/anie.202303296.

6. X. H. Niu, R. Zhao, S. M. Yan, et al., "Chiral Materials: Progress, Applications, and Prospects," *Small* 19 (2023): e2303059, https://doi.org/10.1002/smll.202303059.

7. M. H. Garner and C. Corminboeuf, "Correlation Between Optical Activity and the Helical Molecular Orbitals of Allene and Cumulenes," *Organic Letters* 22 (2020): 8028–8033, https://doi.org/10.1021/acs.orglett.0c02980.

8. Z. X. Li, P. F. Chen, Z. G. Ni, et al., "An Unusual Chiral-at-metal Mechanism for BINOL-metal Asymmetric Catalysis," *Nature Communications* 16 (2025): 735, https://doi.org/10.1038/s41467-025-56000-y.

9. L. Wan, Y. Z. Liu, M. J. Fuchter, and B. H. Yan, "Anomalous Circularly Polarized Light Emission in Organic Light-emitting Diodes Caused by Orbital–momentum Locking," *Nature Photonics* 17 (2022): 193–199, https://doi.org/10.1038/s41566-022-01113-9.

10. Z. A. VanOrman, W. R. Kitzmann, A.-P. M. Reponen, T. Deshpande, H. J. Jöbsis, and S. Feldmann, "Chiral Light–matter Interactions in Solution-processable Semiconductors," *Nature Reviews Chemistry* 9 (2025): 208–223, https://doi.org/10.1038/s41570-025-00690-x.

11. Y. Z. Liu, J. W. Xiao, J. H. Koo, and B. H. Yan, "Chirality-driven Topological Electronic Structure of DNA-Like Materials," *Nature Materials* 20 (2021): 638–644, https://doi.org/10.1038/s41563-021-00924-5.

12. Y. M. He, Y. Z. Cheng, Y. Duan, et al., "Recent Progress of Asymmetric Catalysis From a Chinese Perspective," *CCS Chemistry* 5 (2023): 2685–2716, https://doi.org/10.31635/ccschem.023.202303347.

13. X. T. Liang, W. T. Liang, P. Y. Jin, H. T. Wang, W. H. Wu, and C. Yang, "Advances in Chirality Sensing With Macrocyclic Molecules," *Chemosensors* 9 (2021): 279, https://doi.org/10.3390/chemosensors9100279.

14. B. J. Han, X. D. Yang, and J. Gao, "Chiral Molecular Sensing Based on Spatially Selective Coupling Between Achiral Metasurface and Chiral Molecules," *Journal of Optics* 27 (2025): 035101, https://doi.org/10.1088/2040-8986/adaf3a.

15. C. Zhang, H. T. Hu, C. M. Ma, et al., "Quantum Plasmonics Pushes Chiral Sensing Limit to Single Molecules: A Paradigm for Chiral Biodetections," *Nature Communications* 15 (2024): 2, https://doi.org/10.1038/s41467-023-42719-z.

16. L. Y. Qin, J. Xie, B. T. Wu, et al., "Axially Chiral Nonbenzenoid Nanographene With Second Harmonic Generation Property," *Journal of the American Chemical Society* 146 (2024): 12206–12214, https://doi.org/10.1021/jacs.4c03007.

17. W. L. Shang, Y. Wang, X. F. Zhu, et al., "Helical Cage Rotors Switched on by Brake Molecule With Variable Fluorescence and Circularly Polarized Luminescence," *Journal of the American Chemical Society* 145 (2023): 27639–27649, https://doi.org/10.1021/jacs.3c09461.

18. Y. J. Liu, Z. T. Ma, Z. H. Wang, and W. Jiang, "Boosting Circularly Polarized Luminescence Performance by a Double π-Helix and Heteroannulation," *Journal of the American Chemical Society* 144 (2022): 11397–11404, https://doi.org/10.1021/jacs.2c04012.

19. K. Bian, C. Gerber, A. J. Heinrich, D. J. Müller, S. Scheuring, and Y. Jiang, "Scanning Probe Microscopy," *Nature Reviews Methods Primers* 1 (2021): 36, https://doi.org/10.1038/s43586-021-00033-2.

20. K. Biswas, J. I. Urgel, K. Xu, et al., "On-Surface Synthesis of a Dicationic Diazahexabenzocoronene Derivative on the Au(111) Surface," *Angewandte Chemie International Edition* 60 (2021): 25551–25556, https://doi.org/10.1002/anie.202111863.

21. T. Wang, A. Berdonces-Layunta, N. Friedrich, et al., "Aza-Triangulene: On-Surface Synthesis and Electronic and Magnetic Properties," *Journal of the American Chemical Society* 144 (2022): 4522–4529, https://doi.org/10.1021/jacs.1c12618.

22. J. Holec, B. Cogliati, J. Lawrence, et al., "A Large Starphene Comprising Pentacene Branches," *Angewandte Chemie International Edition* 60 (2021): 7752–7758, https://doi.org/10.1002/anie.202016163.

23. S. Mishra, S. Fatayer, S. Fernández, K. Kaiser, D. Peña, and L. Gross, "Nonbenzenoid High-Spin Polycyclic Hydrocarbons Generated by Atom Manipulation," *ACS Nano* 16 (2022): 3264–3271, https://doi.org/10.1021/acsnano.1c11157.

24. C. Li, Y. Liu, Y. Liu, et al., "Topological Defects Induced High-Spin Quartet State in Truxene-Based Molecular Graphenoids," *CCS Chemistry* 5 (2023): 695–703, https://doi.org/10.31635/ccschem.022.202201895.

25. I. Rončević, F. Paschke, Y. Z. Gao, et al., "A Molecule With Half-Möbius Topology," *Science* (2026): eaea3321, https://doi.org/10.1126/science.aea3321.

26. A. Mugarza, R. Robles, C. Krull, R. Korytár, N. Lorente, and P. Gambardella, "Electronic and Magnetic Properties of Molecule-metal Interfaces: Transition-metal Phthalocyanines Adsorbed on Ag(100)," *Physical Review B* 85 (2012): 155437, https://doi.org/10.1103/PhysRevB.85.155437.

27. H. J. Song, H. Zhu, Z. C. Huang, et al., "Steering the Achiral Into Chiral With a Self-Assembly Strategy," *ACS Nano* 13 (2019): 7202–7208, https://doi.org/10.1021/acsnano.9b02683.

28. J. Ishioka, Y. H. Liu, K. Shimatake, et al., "Chiral Charge-Density Waves," *Physical Review Letter* 105 (2010): 176401, https://doi.org/10.1103/PhysRevLett.105.176401.

29. M. Vilas-Varela, F. Romero-Lara, A. Vegliante, et al., "On-Surface Synthesis and Characterization of a High-Spin Aza-[5]-Triangulene," *Angewandte Chemie International Edition* 62 (2023): e202307884, https://doi.org/10.1002/anie.202307884.

30. D. Skidin, F. Eisenhut, M. Richter, et al., "On-surface Synthesis of Nitrogen-doped Nanographenes With 5–7 Membered Rings," *Chemical Communications* 55 (2019): 4731–4734, https://doi.org/10.1039/C9CC00276F.

31. I. Piskun, R. Blackwell, J. Jornet-Somoza, et al., "Covalent C–N Bond Formation Through a Surface Catalyzed Thermal Cyclodehydrogenation," *Journal of the American Chemical Society* 142 (2020): 3696–3700, https://doi.org/10.1021/jacs.9b13507.

32. Y. Zhang, J. C. Lu, Y. Li, et al., "On-Surface Synthesis of a Nitrogen-Doped Graphene Nanoribbon With Multiple Substitutional Sites," *Angewandte Chemie International Edition* 61 (2022): e202204736, https://doi.org/10.1002/anie.202204736.

33. E. C. H. Wen, P. H. Jacobse, J. W. Jiang, et al., "Magnetic Interactions in Substitutional Core-Doped Graphene Nanoribbons," *Journal of the American Chemical Society* 144 (2022): 13696–13703, https://doi.org/10.1021/jacs.2c04432.

34. X.-Y. Wang, M. Richter, Y. He, et al., "Exploration of Pyrazine-embedded Antiaromatic Polycyclic Hydrocarbons Generated by Solution and On-surface Azomethine Ylide Homocoupling," *Nature Communications* 8 (2017): 1948, https://doi.org/10.1038/s41467-017-01934-1.

15213773, 0, Downloaded from https://onlinelibrary.wiley.com/doi/10.1002/anie.202507878 by Wei Ji - RENMIN UNIVERSITY OF CHINA NON-EAL ACCOUNT, Wiley Online Library on [24/04/2026]. See the Terms and Conditions (https://onlinelibrary.wiley.com/terms-and-conditions) on Wiley Online Library for rules of use; OA articles are governed by the applicable Creative Commons License

35. S. Kawai, S. Nakatsuka, T. Hatakeyama, et al., "Multiple Heteroatom Substitution to Graphene Nanoribbon," *Science Advances* 4 (2018): eaar7181, https://doi.org/10.1126/sciadv.aar7181.

36. O. Krejčí, P. Hapala, M. Ondráček, and P. Jelínek, "Principles and Simulations of High-resolution STM Imaging With a Flexible Tip Apex," *Physical Review B* 95 (2017): 045407.

37. I. Piquero-Zulaica, T. Scharfe, E. Corral-Rascón, et al., "Achiral Electronic Structure Landscapes in Organizationally Chiral Square Nanoporous Networks," *Journal of Physical Chemistry Letters* 16 (2025): 6809–6816, https://doi.org/10.1021/acs.jpclett.5c01385.

38. H. Zhang, M. Pink, Y. Wang, S. Rajca, and A. Rajca, "High-Spin S = 3/2 Ground-State Aminyl Triradicals: Toward High-Spin Oligo-Aza Nanographenes," *Journal of the American Chemical Society* 144 (2022): 19576–19591, https://doi.org/10.1021/jacs.2c09241.

Supporting Information

Additional supporting information can be found online in the Supporting Information section.

Supporting File 1: anie72362-sup-0001-SuppMat.Docx.

15213773, 0, Downloaded from https://onlinelibrary.wiley.com/doi/10.1002/anie.202578978 by Wei Ji - RENMIN UNIVERSITY OF CHINA NON-EAL ACCOUNT , Wiley Online Library on [24/04/2026]. See the Terms and Conditions (https://onlinelibrary.wiley.com/terms-and-conditions) on Wiley Online Library for rules of use; OA articles are governed by the applicable Creative Commons License